Multimode VCSEL model for wide frequency-range RIN simulation

Julien Perchoux, Angélique Rissons, Jean-Claude Mollier

Multimode VCSEL model for wide frequency-range RIN simulation

Julien Perchoux [a,*], Angélique Rissons [b], Jean-Claude Mollier [b]

[a] ENSEEIHT, 2 Rue C. Camichel, Toulouse, France
[b] MOSE Laboratory, Supaero, 10 Av. E. Belin, Toulouse, France

Abstract

In this paper, we present an equivalent circuit model for oxide-confined AlGaAs/GaAs VCSEL with the noise contribution adapted to optomicrowave links applications. This model is derived from the multimode rate equations. In order to understand the modal competition process, we restrain our description to a two-modes rate equations system affected by the spectral hole-burning. The relative intensity noise (RIN) measurements which were achieved on a prober in Faraday cage confirm the low frequency enhancement described by the model. We validate our model for a wide frequency-range [1 MHz–10 GHz] and high bias level up to six times the threshold current.

Keywords: VCSEL; Rate equations; Modeling; RIN; Equivalent circuit; Multimode laser diode

1. Introduction

The well-known advantages of VCSELs have been leading to a quick increasing of the application domains for these emitters. To follow that growing diversity it is necessary to develop various VCSEL structures [1], with output power enhancement, wavelength shifting towards fiber telecoms range, or single transverse-mode emission. However, some of these advantages are until present quite incompatible. In particular, single transverse-mode emission and output power enhancement are antagonist properties for both proton-implanted and oxide-confined devices. For example, in oxide-confined VCSELs, the high effective index step induced by the oxide aperture is a source of multimodal emission. As a result, only small oxide-aperture diameter (lower then 3 μm) are susceptible to allow single-mode emission while output power is an increasing function of the diameter [2]. Another drawback of the singlemode VCSELs production is the manufacturing difficulties such as the precise control of the aperture diameter or the electrostatic discharge sensitivity (ESD) which is due to the small size of the device [3].

For all these reasons, most commercial VCSELs are multimode-transverse oxide-aperture devices [4]. Many previous works demonstrate the optical properties degradations which is caused by the mode competition in both edge-emitting lasers [5,6] and VCSELs [7–10]. The noise increase for frequencies less than 500 MHz is the most important consequence of the mode competition. So, a rigorous description of that behavior would involve to model precisely the emission of transverse modes, their spatial distribution and its evolution against bias current and VCSEL cavity temperature. But, due to the specific VCSEL geometry and the induced spatial hole-burning, the emitted modes feature a complex spatial distribution which is a characteristic of each structure. We have studied various oxide-confined VCSELs with a diameter ranging from 6 to 25 μm. Above the threshold, each device featured a ''corolla-like'' near-field distribution which is very different from any gaussian mode LPmn. That typical result for oxide-confined VCSELs [4] needs a complex spatial modeling [11]. The increase of noise that we may observe with that type of VCSEL structure for frequency decreasing

* Corresponding author. Tel.: +33 5 61 58 84 36.
E-mail addresses: julien.perchoux@enseeiht.fr (J. Perchoux), angelique.rissons@supaero.fr (A. Rissons), jean-claude.mollier@supaero.fr (J.-C. Mollier).

under 500 MHz, reaches a plateau up to 20 dB according to the bias current and the cavity geometry. That noise evolution is similar to the one measured on edge-emitting lasers, so we adopted the same way of mode competition modeling based on spectral hole burning, following what has been done for those laser diodes [12,13]. We do not need to precisely know the spatial distribution of transverse modes, especially as, for well-above threshold bias currents (what is usually the case in most applications), the transverse modes density leads to a mode overlap around the periphery of the VCSEL active area.

We present, in a first part, a multimode signal and noise VCSEL model based on the rate equations for carriers and photons. This model takes into account the mode competition through the gain non-linearity of the active area. Then, after a brief presentation of the singlemode VCSEL model including Langevin sources, we introduce the multimode rate equations characterized by a non-linear gain which describes the mode competition due to the spectral hole-burning. In a third part, we present the linearization of a two-mode rate equation system which allows the building of both signal and noise electrical equivalent model. Finally, the electrical model is simulated through a CAD software and simulation results are compared to RIN measurements realized for a wide frequency range (from 1 MHz up to 10 GHz) at various injection current levels.

2. VCSEL specific rate equations

2.1. VCSEL monomodal rate equations

The monomodal VCSEL rate equations for the electron number N in each quantum well and the photon number P in the emitted mode, can be written as [14]:

$$\frac{\mathrm{d}N}{\mathrm{d}t} = \frac{\eta_i I}{qN_\mathrm{w}} - (A + \mathrm{BN})N - GP + F_\mathrm{N}(t) \tag{1a}$$

$$\frac{\mathrm{d}P}{\mathrm{d}t} = N_\mathrm{w}\mathrm{GP} + N_\mathrm{w}\Gamma\beta\mathrm{BN}^2 - \frac{P}{\tau_\mathrm{p}} + F_\mathrm{P}(t) \tag{1b}$$

In these equations, $\frac{\eta_i I}{qN_\mathrm{w}}$ represents the injection of carriers due to the current I in N_w quantum wells with the quantum efficiency η_i. $(A + \mathrm{BN})N$ represents the sum of the non-radiative recombinations (AN) and the spontaneous emission (BN^2); taking into account the short emission wavelength, the Auger effect has been neglected.

The term $N_\mathrm{w}\Gamma\beta\mathrm{BN}^2$ describes the part of the spontaneous emission involved in the emitted mode, β is called spontaneous emission factor and Γ is the optical confinement factor. The term $\frac{P}{\tau_\mathrm{p}}$ takes into account the global photon loss, with τ_p the photon lifetime in the cavity.

GP is the difference between stimulated emission and stimulated absorption. The gain G of the active area can be expressed as [14]:

$$G = g_0 \frac{N - N_\mathrm{tr}}{1 + \epsilon P} \tag{2}$$

with N_tr the electrons number at transparency, ϵ the gain compression factor and $g_0 = v_\mathrm{gr}\Gamma\frac{a}{V_\mathrm{act}}$ a factor depending on Γ, the group velocity v_gr, the differential gain a and the volume of the active area V_act.

Finally, the functions $F_\mathrm{N}(t)$ and $F_\mathrm{P}(t)$ are the well-known Langevin forces and describe the stochastic evolution of the photon and electron populations. We used the description of Harder et al. [15] based on McCumber's model [16] to express their spectral densities and cross correlation functions from the intrinsic parameters of the VCSEL as:

$$\left\langle F_\mathrm{N}(t)^2 \right\rangle = \sum r_\mathrm{N}^+ + \sum r_\mathrm{N}^- \tag{3a}$$

$$\left\langle F_\mathrm{P}(t)^2 \right\rangle = \sum r_\mathrm{P}^+ + \sum r_\mathrm{P}^- \tag{3b}$$

$$\langle F_\mathrm{N}(t)F_\mathrm{P}(t)\rangle = -\left[\sum r_\mathrm{NP} + \sum r_\mathrm{PN}\right] \tag{3c}$$

In these equations, r_N^+ and r_N^- are the rate of increasing and decreasing electron population, r_P^+ and r_P^- are the equivalent rate for the photon population and the terms r_NP and r_PN are the rate of exchanges between the two reservoirs.

We have used Eqs. (1a) and (1b), for a steady state defined by the average values $\overline{I}, \overline{N}$ and $\overline{P}$, to express a simplified form of Eqs. (3a)–(3c) as follows:

$$\left\langle F_\mathrm{N}(t)^2 \right\rangle = 2\, g_0 \frac{N_\mathrm{tr}}{1 + \epsilon\overline{P}}\overline{P} + \frac{\eta_i \overline{I}}{qN_\mathrm{w}} \tag{4a}$$

$$\left\langle F_\mathrm{P}(t)^2 \right\rangle = 2N_\mathrm{w} g_0 \frac{N_\mathrm{tr}}{1 + \epsilon\overline{P}}\overline{P} + \frac{2\overline{P}}{\tau_\mathrm{p}} \tag{4b}$$

$$\langle F_\mathrm{N}(t)F_\mathrm{P}(t)\rangle = -\left[2g_0 \frac{N_\mathrm{tr}}{1 + \epsilon\overline{P}}\overline{P} + \frac{\overline{P}}{\tau_\mathrm{p}}\right] \tag{4c}$$

We have presented in [14] several simulation results of this behavioral model in signal and noise with worth results at frequencies from 1 GHz to 10 GHz. A depth study of multimode oxide-confined VCSELs with various aperture diameters shows the strong influence of the multimodal emission on the RIN at lower frequencies. As the single-mode model predict a white gaussian noise at frequencies between 10 kHz and a few gigaherz, noise measurements realized on transverse multimode VCSELs demonstrates the necessity to extend our model to take into consideration multimodal behavior of VCSELs.

2.2. Mode competition in oxide-confined VCSELs

As it has been shown by several authors [5,6], mode competition in semi-conductor lasers leads to relative intensity noise enhancement at low frequencies under 1 GHz. Most of the VCSELs available until now are transverse multimode devices. Massive use of monomode VCSELs is still limited by lower emission power characteristics. This is due to the strong geometric conditions of monomode emission which leads to thinner structures with a strong limitation of the available emitted power.

It has been demonstrated that VCSEL modal emission strongly depends on the optical confinement method [17]. In all our studies, we have worked exclusively on multiple quantum well oxide-confined VCSELs designed by ULM photonics. For that kind of structures, two main parameters affect the modal behavior: the oxide-aperture diameter and the injection current.

For the latest, it is a result of inhomogeneity and nonlinearities at high bias level. Measurements on a 12 μm oxide-aperture VCSEL for two different injection levels are presented in Fig. 1.

The oxide-aperture diameter is the main factor that affects the modal emission. In particular, measurements performed on VCSELs with oxide aperture diameter varying from 6 μm to 25 μm show an increasing number of modes with the aperture diameter. The VCSELs are still low-emitted power devices comparatively to conventional edge-emitters. To increase their power it is necessary to design a large oxide-aperture diameter [2]. For numerous applications, where sufficient power is needed, multimode VCSELs can not be replaced by singlemode devices. So the study of modes interactions in such laser diodes and their effects on the emission properties is still a subject of great interest.

Another specific behavior of the oxide-aperture VCSELs comes from the carrier distribution in the active area. It has been shown [11] that the cylindrical structure of the oxidized layer leads to a ring-shaped concentration of carriers. The result of such a carrier distribution is the enhancement of the transverse modes at the edge of the emitting area. Above threshold, the Gaussian fundamental mode could be neglected in regard of the main transverse modes intensity.

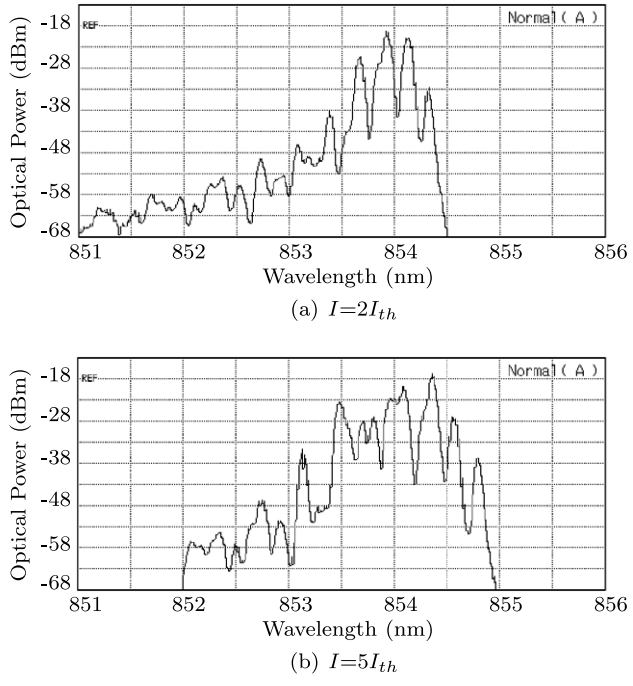

Fig. 1. Optical spectrum of a 12 μm oxide-aperture VCSEL at (a) $2I_{\text{th}}$ and (b) $5I_{\text{th}}$ (with I_{th} the threshold current).

2.3. Multimodal rate equations

Because of the particular VCSEL structure, the modal gain is affected by both spatial and spectral hole-burning. A rigorous physical treatment of the mode competition phenomena should take into account both interactions types. It is generally accepted in the literature that spatial hole-burning greatly affect the behavior in signal and RIN of multiple transverse modes VCSELs. Previous studies have developed a spatial hole-burning based model for mode competition in VCSELs [10,18,19]. Nevertheless, describing the spatial profile of the lasing wave in the active region is not easy as that profile is strongly dependent of many parameters such as the thermal diffusion, the hazardous geometry of the optical guide in the cavity. Moreover, for relatively large oxide-aperture (above 10 μm), with numerous emitted modes, the spatial distribution should be described by complex mathematical functions. We have considered, in a first approximation, that a model based on spectral hole-burning would be able to simulate efficiently the behavior of multiple transverse modes VCSELs. In this hypothesis, we assumed that in such wide aperture devices, spatial overlapping is present at a high level. Our model is based on previous works achieved on multimode edge-emitting lasers that present a RIN level enhancement at low frequency similar of the one observed for VCSELs [12,13]. Then, for taking into account the mode competition, the gain for the mode m will be expressed as:

$$G_m = g_0 \frac{N - N_{\text{tr}}}{1 + \epsilon P_m + \sum_{m \neq n} (\epsilon_{mn} P_n)} \tag{5}$$

where the term ϵ_{mn} is the gain compression factor for the mode n due to the mode m. We applied the formalism developed by Manning et al. [13] to express this factor:

$$\epsilon_{mn} = \epsilon \frac{1 + \alpha \tau_{\text{p}} \Omega_{mn}}{1 + (\tau_{\text{p}} \Omega_{mn})^2} \tag{6}$$

In (6), α is the Henry factor relative to the spectral linewidth and $\Omega_{mn} = |\omega_m - \omega_n|$ is the frequency difference between the m and n modes. The gain degradation due to neighbor modes strongly depends on this interval. For taking into account the effect of spatial hole-burning on the mode competition, the ϵ_{mn} parameter defined in (6) should be affected by a spatially dependent function describing the mode overlapping level.

For further applications, it is necessary to develop and simplify the expression of the modal gain given in (5) as:

$$G_m = g_{0m}(N - N_{\text{tr}}) \tag{7}$$

with

$$g_{0m} = g_0 - \kappa_0 P_m - \sum_{m \neq n} \kappa_{mn} P_n \tag{8}$$

where $\kappa_0 = \epsilon g_0$, $\kappa_{mn} = \epsilon_{mn} g_0$.

With that gain expression, the rate equations on the global electrons and photons numbers of each mode become:

$$\frac{dN}{dt} = \frac{\eta_i I}{qN_w} - (A + BN)N - \sum_m G_m P_m + F_N(t) \tag{9a}$$

$$\frac{dP_m}{dt} = N_w G_m P_m + N_w \Gamma \beta B N^2 - \frac{P_m}{\tau_p} + F_m(t) \tag{9b}$$

We did the same way as for the monomodal VCSEL model in (4), we expressed the spectral density and cross correlation of the Langevin functions with the modal gain developed in (7):

$$\left\langle F_N(t)^2 \right\rangle = \sum_m 2\overline{g_{0m}} N_{tr} \overline{P_m} + \frac{\eta_i \overline{I}}{qN_w} \tag{10a}$$

$$\left\langle F_m(t)^2 \right\rangle = 2N_w \overline{g_{0m}} N_{tr} \overline{P_m} + \frac{2\overline{P_m}}{\tau_p} \tag{10b}$$

$$\langle F_N(t) F_m(t) \rangle = 2N_w \overline{g_{0m}} N_{tr} \overline{P_m} + \frac{\overline{P_m}}{\tau_p} \tag{10c}$$

We considered that the cross correlation functions between the Langevin functions for photons of each mode is equal to zero, as there is no direct interaction between these populations.

3. Electrical equivalent model

Building an electrical equivalent model is of great interest for the modeling of the active area behavior in both noise and signal dynamics. First, it allows implementation in usual software for electrical simulations. Second it can be completed by an electrical behavioral model of the Bragg reflectors, so one can simulate the global VCSEL behavior. The laser diode can be simulated in a complete electrical environment. Finally, thanks to the limitation of the electrical elements and the restrictions of these parameters values to realistic ranges, the electrical equivalent circuit reduces the influence of the numerous intrinsic parameters on simulation. It allows easier and reliable optimization of the device.

3.1. Small-signal linearized two-mode rate equations

3.1.1. Two-mode approximation

For an easier handling of the dynamic rate equations of the VCSELs, it is necessary to simplify them.

At first, we propose to limit the model by taking into account only two modes. The main argument for that simplification lies in the κ_{mn} dependence on the frequency difference Ω_{mn} between the modes as described in (6): the mutual perturbation of two closed modes is by far the strongest one compared to the reciprocal influence of two other modes, which is then neglected in a first approximation.

Secondly as we explained in 2.2, the VCSEL features a multimode transverse behavior. In edge-emitter, multimodal emission effects are due to the action of weak transverse modes on the main Gaussian mode. In VCSELs, due to their particular geometry, transverse modes acts on other transverse modes, so we can consider that the reciprocal interactions are symmetric, as none is specific, for its intensity or its shape.

For these two reasons, we suppose that a two-mode model is sufficient to describe the main influences of the modal competition on the diode behavior.

From (6) the interaction between the modes 1 and 2 is described by:

$$\kappa_{12} = \kappa_0 \frac{1 + \alpha \tau_p \Omega_{12}}{1 + (\tau_p \Omega_{12})^2} \tag{11}$$

As $\Omega_{12} = \Omega_{21}$, we can note $\kappa = \kappa_{12} = \kappa_{21}$ and the Eq. (8) becomes:

$$g_{0m} = g_0 - \kappa_0 P_m - \kappa P_n \tag{12}$$

With such a simplification, we can simulate the evolution of the Langevin functions spectral densities according to the injection current.

3.1.2. Small-signal linearization

To take into account the dynamics of the rate Eqs. (9), the state parameters I, N and P_m can be developed as:

$$I = \overline{I} + \Delta I \tag{13a}$$

$$N = \overline{N} + \Delta N \tag{13b}$$

$$P_m = \overline{P_m} + \Delta P_m \tag{13c}$$

and the result of first order linearization for rate equations is:

$$\frac{d\Delta N}{dt} = \frac{\eta_i}{qN_w} \Delta I - \Gamma_N \Delta N - \sum_m G'_m \Delta P_m + F_N(t) \tag{14a}$$

$$\frac{d\Delta P_m}{dt} = K_m \Delta N + \Gamma_m \Delta P_m - \gamma_{mn} \Delta P_n + F_m(t) \tag{14b}$$

where Γ_N, G'_m, K_m, Γ_m and γ_{mn}, are constant terms only depending on steady state variables $\overline{I}, \overline{N}$ and $\overline{P_m}$ (see Appendix A).

Compared to single mode linearized rate equations, the significant result stays in the γ_{mn} term which links the evolution of one mode photon population to the photon population of the other one. This interaction is clearly expressed by the equivalent circuit of the active area.

3.2. Two-mode electrical equivalent circuit

To link the small-signal linearized rate equations to the small-signal electrical equations of an equivalent circuit, we used the classical relation given in [20,21] between small signal junction voltage ΔV and electron population variation ΔN given in (15):

$$\Delta V = m V_T \frac{\Delta N}{\overline{N}} \tag{15}$$

with m the junction ideality coefficient and V_T the thermal voltage.

The linearized rate equations system in (14) can be identified to the electrical equation system (16) derived from applying Kirchoff laws in the equivalent circuit presented in Fig. 2.

$$\frac{\mathrm{d}\Delta V}{\mathrm{d}t} = \frac{\Delta I + i_N}{C_\mathrm{j}} - \frac{\Delta V}{R_\mathrm{j} C_\mathrm{j}} - \sum_m \frac{i_{L_m}}{C_\mathrm{j}} \tag{16a}$$

$$\frac{\mathrm{d}i_{L_m}}{\mathrm{d}t} = \frac{\Delta V}{L_m} - \frac{V_{mn}}{L_m} - \frac{r_m}{L_m} i_{L_m} - \frac{v_{N_m}}{L_m} \tag{16b}$$

with $V_{mn} = M_{mn} i_n$.

This equivalent circuit is composed of a R_j–C_j–i_N parallel element describing the junction behavior of the active area. The inductive branches are linked to the photon population and the interaction between modes is represented by the controlled voltage sources V_{mn}. Direct analogy between Eqs. (14) and (16) gives firstly the relations between small-signal current variation in each inductive branch and variation of the photon number in each mode:

$$i_{L_m} = \frac{q N_\mathrm{w}}{\eta_i} G'_m \Delta P_m \tag{17}$$

In a second time, it allows identification of every single parameter:

$$C_\mathrm{j} = \frac{q N_\mathrm{w} \overline{N}}{\eta_i m V_\mathrm{T}} \tag{18a}$$

$$R_\mathrm{j} = \left(\Gamma_\mathrm{N} C_\mathrm{j}\right)^{-1} \tag{18b}$$

$$L_m = \left(G'_m K_m C_\mathrm{j}\right)^{-1} \tag{18c}$$

$$r_m = \Gamma_m L_m \tag{18d}$$

$$M_{mn} = \frac{\gamma_{mn}}{K_m C_\mathrm{j} G'_n} \tag{18e}$$

The simulation results of these parameters values evolution against the injected current and the relative importance of the first mode on the second are illustrated in Fig. 3. As we can see, equivalent inductances and resistances are decreasing functions of the injection current as well as of the photon population in the mode (Eqs. (3a) and (3b)). The equivalent transimpedances which are increasing functions of the current are not influenced by the relative photon densities in each mode (Fig. 3c).

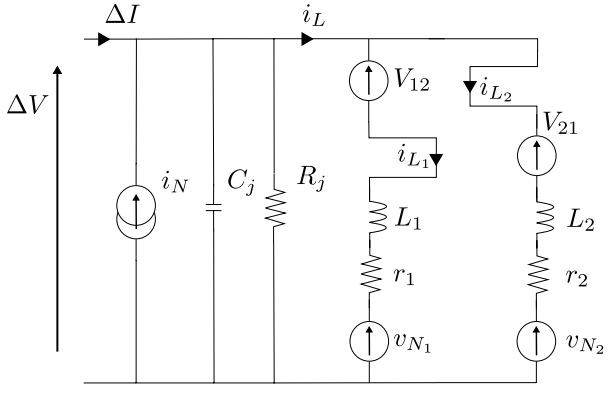

Fig. 2. Two-mode electrical equivalent circuit of a VCSEL active area (with $V_{12} = M_{12} \cdot i_{L_2}$ and $V_{21} = M_{21} \cdot i_{L_1}$).

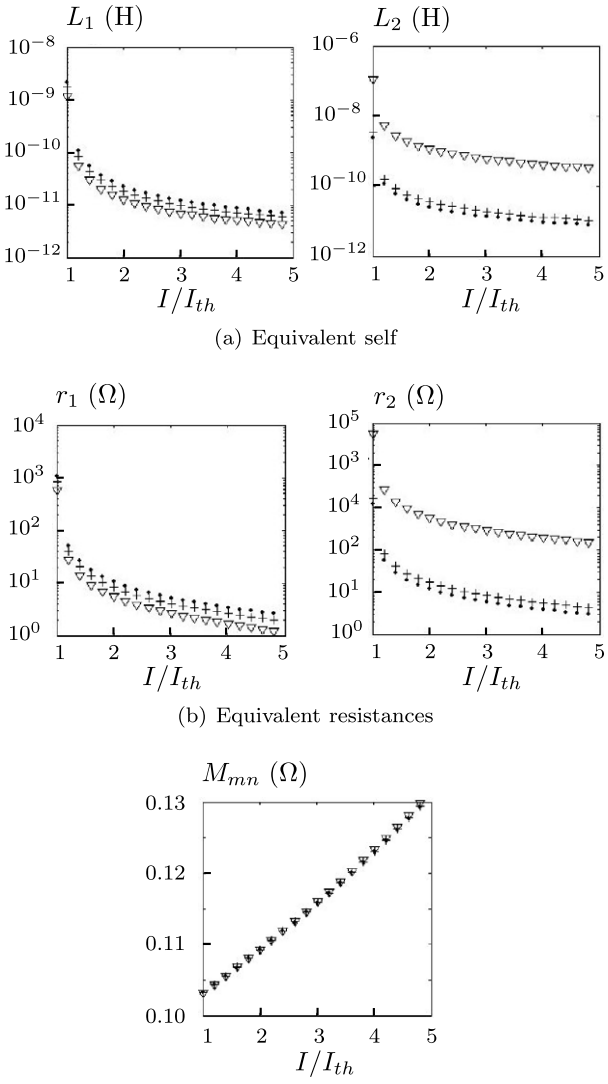

Fig. 3. Evolution of electrical equivalent parameters against normalized bias current for different values of P_1/P_2 (dotted-lines: $P_2 = 0.9P_1$, +lines: $P_2 = 0.5P_1$, Vlines: $P_2 = 0.01P_1$).

Finally, the equivalent electrical noise sources spectral densities can be expressed as functions of the spectral densities of the Langevin functions as:

$$i_N^2 = \left(\frac{q N_\mathrm{w}}{\eta_i}\right)^2 F_\mathrm{N}^2 \tag{19a}$$

$$v_{N_m}^2 = \left(\frac{\eta_i m V_\mathrm{T}}{K_m \overline{N}}\right)^2 F_m^2 \tag{19b}$$

The evolutions of these spectral densities against the injection current and the relative photon densities are presented in Fig. 4. If the spectral density of the equivalent current source is an increasing function of the injection current, it is weakly affected by the variations of the photon population ratio (Fig. 4a). On the contrary, spectral densities of

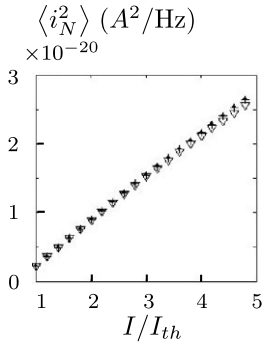

(a) Equivalent noise current source spectral density

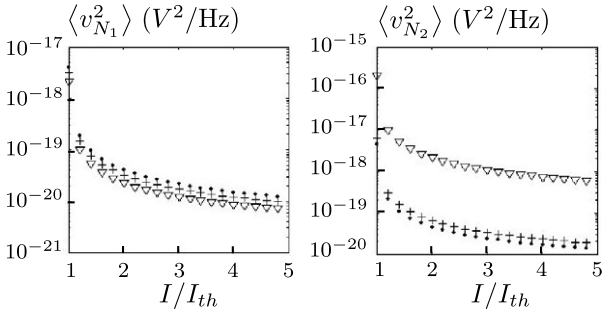

(b) Equivalent noise voltage source spectral densities

Fig. 4. Evolution of equivalent noise sources spectral densities against normalized bias current for different values of P_1/P_2 (dotted-lines: $P_2 = 0.9P_1$, +lines: $P_2 = 0.5P_1$, ∇lines: $P_2 = 0.01P_1$).

voltage sources are decreasing functions of the injection current and they are more significant for lower population levels (Fig. 4b).

4. Measurements

4.1. Measurement setup

Numerous VCSELs with various aperture diameters (from 6 μm to 25 μm) have been tested. These devices were 850 nm AlGaAs VCSELs designed by ULM Photonics. The experimental setup is presented in Fig. 5. Electrical access to the chip was realized by coplanar probes. The laser light was collected trough a lensed multimode fiber. All measurements have been performed in a Faraday cage, the injected current beeing supplied by an ILX ultra-low noise laser driver. A New Focus 12 GHz photodetector have been used, it is composed by a InGaAs PIN photodiode, a 60 dB transimpedance amplifier and an output for DC voltage measurements.

4.2. Model validation

Measurements have been made over a wide frequency-range, from 1 MHz to 10 GHz and for various bias levels (from 1.1 to 6 time the threshold current). Results are presented in Fig. 6. We observe an usual behavior at high frequencies, with a resonant peak decreasing and moving to

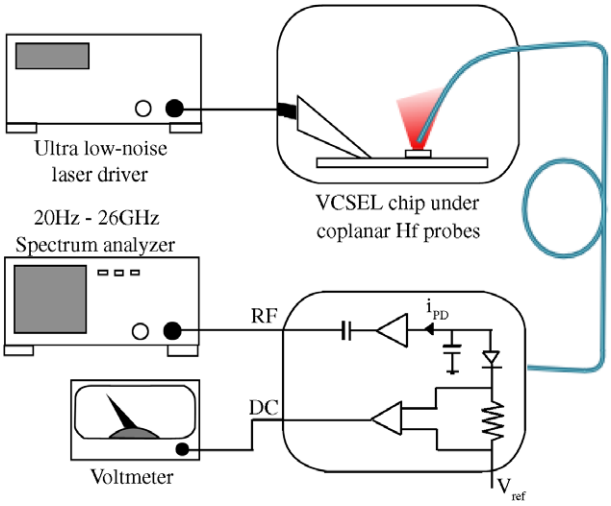

Fig. 5. Experimental setup for noise measurements on VCSELs.

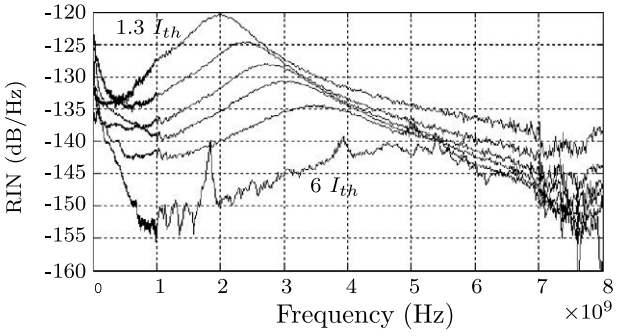

Fig. 6. RIN of 12 μm oxide-aperture VCSEL under various bias currents (1.3, 1.7, 2, 2.5, 3 and 6 times I_{th}) – Linear frequency scale.

higher frequencies when bias current gets higher. At lower frequencies range, we notice a RIN level enhancement of several decibels, which is due to mode competition. This phenomenon is more obvious with a logarithmic frequency scale (Fig. 7).

Those measurements have been compared to a complete simulation of the VCSELs including the active area equivalent circuit model and a Bragg reflector electrical model [14].

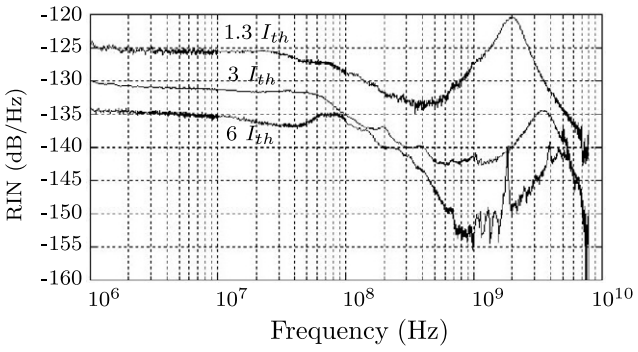

Fig. 7. RIN of 12μm oxide-aperture VCSEL under various bias currents (1.3, 3 and 6 times I_{th}) – logarithmic frequency scale.

The range for the intrinsic parameters values used to calculate the active area electrical elements is presented in Table 1. The electrical parameters are then optimized, with easy handling allowed by the CAD software, with respect to this range. Extracting the values by fitting simulated data and experimental curves (Fig. 8) we obtained the equivalent parameters given in Table 2. It can be seen that the variation of these parameters against the bias current is consistent with the simulations illustrated in Figs. 3 and 4.

Results presented in Fig. 8 demonstrate an excellent agreement at high frequencies close to the resonant peak and up to 8 GHz, as well as at lower frequencies where mode competition is observed. As it can be seen in Fig. 8, at high bias levels, curves are presenting incoherent behavior which could not be taken into account with our simplified two-mode model. We think that it could be the consequence of multiple interactions between numerous modes in the cavity as suggested by Valle and Pesquera [18].

Table 1
Intrinsic parameters values

Parameters	Symbol	Value	Unit
Non-radiative recombinations	A	$[1–1.3]\times 10^{8}$	s^{-1}
Spontaneous emission	$B\times V_{act}$	$[0.7–1.8]\times 10^{-16}$	$m^3\,s^{-1}$
Transparency carriers density	$\frac{N_{tr}}{V_{act}}$	$[0.83–4.4]\times 10^{24}$	m^{-3}
Photon lifetime	τ_P	[1–6]	ps
Differential gain term	a	$[0.2–3.7]\times 10^{-20}$	m^2
Group velocity	v_{gr}	$[8.33–8.6]\times 10^{7}$	$m\,s^{-1}$
Confinement factor	Γ	$[4.5–6]\times 10^{-2}$	$m\,s^{-1}$
Spontaneous emission factor	β	$[1–10]\times 10^{-5}$	–
Quantum efficiency	η_i	$[6–8.6]\times 10^{-1}$	–
Compression factor	ϵ	$[2–4]\times 10^{-6}$	–
Linewidth enhancement factor	α	[2–8]	–

Sources: [4,9,17,11,20,22–30]

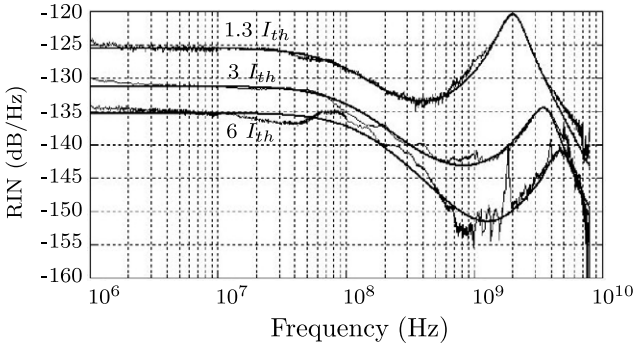

Fig. 8. Comparison of simulation and measurements of RIN for a 12 μm oxide-aperture VCSEL under various bias currents (1.3, 3 and 6 times I_{th}) – logarithmic frequency scale.

Table 2
Equivalent circuit model parameters

Parameter	$I=1.5I_{th}$	$I=3I_{th}$	$I=6I_{th}$
C_j (pF)	36.4	28.7	24.3
R_j (Ω)	5.8	3.8	3.7
L_1 (pH)	200	85	52
L_2 (mH)	1157	478	367
r_1 (Ω)	0.252	0.25	0.235
r_2 (Ω)	0.527	0.132	0.124
M_{12} (Ω)	1.06	1.12	1.26
M_{21} (Ω)	1.08	1.09	1.25
i_N ($pA/\sqrt{Hz}$)	Indifferent		
v_{N_1} ($nV/\sqrt{Hz}$)	2.7	3	3.4
v_{N_2} ($nV/\sqrt{Hz}$)	2.6	4.9	7

5. Conclusion

Rate equations of a multiple transverse-mode VCSEL have been established. They take into account the mode competition due to spectral hole-burning. This model has been simplified to a two-mode signal and noise model which allows small-signal linearization of the rate equations. An equivalent electrical model of the active area has been developed allowing a more precise simulation of the laser behavior in dynamic regime. Finally RIN measurements on a wide frequency-range (from 1 MHz up to 10 GHz) have validated the model with a good agreement. The simplification of the equations allows easy handling of the model and demonstrates a good estimation of the RIN over the frequency-range even at high injection levels where more complex mode-interactions are expected. The equivalent electrical model should allow to perform a complete electrical circuit model of VCSELs including Bragg reflectors and AlO_x aperture behavioral circuit.

Acknowledgement

The authors would like to thank Dr. Martin Grabherr at ULM Photonics for providing VCSELs and numerous informations.

Appendix A. Development of multimode rate equations linearization

From the Eqs. (9) and (13), by taking into account only two modes and using a partial derivation method, we can write:

$$\frac{d}{dt}[\Delta N(I,N,P_1,P_2] = \Delta\dot{N} = \frac{\partial\dot{N}}{\partial I}\Delta I + \frac{\partial\dot{N}}{\partial N}\Delta N + \frac{\partial\dot{N}}{\partial P_1}\Delta P_1 + \frac{\partial\dot{N}}{\partial P_2}\Delta P_2 \quad \text{(A.1a)}$$

$$\frac{d}{dt}[\Delta P_1(I,N,P_1,P_2] = \Delta\dot{P}_1 = \frac{\partial\dot{P}_1}{\partial I}\Delta I + \frac{\partial\dot{P}_1}{\partial N}\Delta N + \frac{\partial\dot{P}_1}{\partial P_1}\Delta P_1 + \frac{\partial\dot{P}_1}{\partial P_2}\Delta P_2 \quad \text{(A.1b)}$$

$$\frac{d}{dt}[\Delta P_2(I,N,P_1,P_2] = \Delta\dot{P}_2 = \frac{\partial\dot{P}_2}{\partial I}\Delta I + \frac{\partial\dot{P}_2}{\partial N}\Delta N + \frac{\partial\dot{P}_2}{\partial P_1}\Delta P_1 + \frac{\partial\dot{P}_2}{\partial P_2}\Delta P_2 \quad \text{(A.1c)}$$

With this method, we propose to define each element in (A.1) as:

$$\Gamma_{\mathrm{N}} = \frac{\partial \dot{N}}{\partial N} \tag{A.2a}$$

$$\Gamma_m = \frac{\partial \dot{P}_m}{\partial P_m} \tag{A.2b}$$

$$K_m = \frac{\partial \dot{P}_m}{\partial N} \tag{A.3}$$

$$G'_m = \frac{\partial \dot{N}}{\partial P_m} \tag{A.4}$$

and

$$\gamma_{mn} = \frac{\partial \dot{P}_m}{\partial P_n} \tag{A.5}$$

The parameters defined in Eqs. (A.2)–(A.5) can be derived directly from the rate Eqs. (9) as:

$$\Gamma_N = A + 2B\overline{N} + \sum_m \overline{g_{0m} P_m} \tag{A.6a}$$

$$\Gamma_m = N_{\mathrm{w}}(\overline{N} - N_{\mathrm{tr}})(g_0 - 2\kappa_0 \overline{P_m} - \kappa \overline{P_n} - \frac{1}{\tau_{\mathrm{p}}} \tag{A.6b}$$

$$K_m = N_{\mathrm{w}} \overline{g_{0m} P_m} + 2N_{\mathrm{w}} \Gamma \beta B \overline{N} \tag{A.7}$$

$$G'_m = \overline{G_m} - \kappa_0(\overline{N} - N_{\mathrm{tr}})\overline{P_m} - \kappa(\overline{N} - N_{\mathrm{tr}})\overline{P_n} \tag{A.8}$$

and

$$\gamma_{mn} = \kappa N_{\mathrm{w}}((\overline{N} - N_{\mathrm{tr}})\overline{P_m} \tag{A.9}$$

Finally, the terms derived from the current I are obvious:

$$\frac{\partial \dot{N}}{\partial I} = \frac{\eta_i}{q N_{\mathrm{w}}} \tag{A.10a}$$

$$\frac{\partial \dot{P}_m}{\partial I} = 0 \tag{A.10b}$$

References

[1] R. Szweda, III-Vs Review 19 (1) (2006) 34.
[2] M. Grabherr, M. Miller, R. Jager, D. Wiedenmann, R. King, VCSEL VIII, in: Proc. SPIE, vol. 5364, p. 174, 2004.
[3] D. Wiedenmann, M. Grabherr, R. Jager, R. King, Vertical-cavity surface-emitting lasers X, in: Proc. SPIE, vol. 6132, p. 1, 2006.
[4] C. Degen, I. Fischer, W. Elsäßer, Opt. Exp. 5 (3) (1999) 38.
[5] G.P. Agrawal, N.K. Dutta, Semiconductors Lasers, second ed., Van Nostrand Reinold, 1993.
[6] K. Petermann, Laser Diode Modulation and Noise, Kluwer, 1988.
[7] G. Giacomelli, F. Marin, M. Grabrysch, K.H. Gulden, M. Moser, Opt. Commun. 146 (1998) 136.
[8] D.V. Kuksenkov, H. Temkin, S. Swirhun, Appl. Phys. Lett. 67 (15) (1995) 2141.
[9] J.Y. Law, G.P. Agrawal, IEEE Photonic. Technol. Lett. 9 (4) (1997) 437.
[10] L.-G. Zei, S. Ebers, J.-R. Kropp, K. Petermann, IEEE J. Lightwave Technol. 19 (6) (2001) 884.
[11] H. Zhang, G. Mrozynski, A. Wallrabenstein, J. Schrage, IEEE J. Quantum electr. 40 (1) (2004) 18.
[12] G.P. Agrawal, Phys. Rev. A 37 (7) (1988) 2488.
[13] J. Manning, R. Olshansky, D.M. Fye, W. Powazinik, Electr. lett. 21 (1985) 496.
[14] A. Rissons, J. Perchoux, J-C. Mollier, M. Grabherr, VCSEL VIII, in: Proc. SPIE, vol. 5364, No. 09, p. 80, San José Photonics West, 2004.
[15] C. Harder, J. Katz, S. Margalit, J. Shacham, A. Yariv, IEEE J. Quantum electr. qe-18 (3) (1982) 333.
[16] D.E. McCumber, Phys. Rev. 141 (1966) 306.
[17] S.F. Yu, Analysis and Design of Vertical Cavity Surface Emitting Lasers, WILEY, 2003.
[18] A. Valle, L. Pesquera, IEEE J. Quantum Electr. 40 (6) (2004) 597.
[19] Y. Satuby, M. Orenstein, IEEE J. Quantum Electr. 35 (6) (1999) 944.
[20] H. Li, K. Iga, Vertical Cavity Surface Emitting Lasers Devices, Springer, 2003.
[21] R.S. Tucker, D.J. Pope, IEEE Trans. Microw. Theory MTT-31 (3) (1983) 289.
[22] P.V. MENA, PhD. Thesis, University of Illinois at Urbana-Champaign, 1998.
[23] X. Li, T.E. Sale, G. Knowles, VCSEL VI, Proc. SPIE, vol. 4649, p. 257, 2002.
[24] T.E. Sale, Vertical Cavity Surface Emitting Lasers, Research Studies Press LTD, 1995.
[25] L.A. Coldren, S.W. Corzine, Diode Lasers and Photonic Integrated Circuits, John Wiley & Sons, 1995.
[26] Y. Liu, W. Ng, F. Oyafuso, B. Klein, K. Hess, Physics and simulation of optoelectronic devices X, in: Proc. SPIE, vol. 4649, p. 190, 2002.
[27] A. Valle, J. Lopez, L. Pesquera, S. Turovets, Physics and simulation of optoelectronic devices X, in: Proc. SPIE, vol. 4649, p. 215, 2002.
[28] M. Bruensteiner, G.C. Papen, IEEE J. Sel. Topics Quantum Electr. 5 (3) (1999) 487.
[29] B.P.C. Tsou, D.L. Pulfrey, IEEE J. Quantum Electr. 33 (2) (1997) 246.
[30] S.C. Kan, K.Y. Lau, IEEE Photonic. Technol. Lett. 4 (6) (1992) 528.